ScienceDirect®

Full Length Article

Polyaniline impact on graphitic C_3N_4's structural and physicochemical properties for high stability energy storage systems: Practical and theoretical studies

Khaled Faisal Qasim [a] 👤 ✉ , Samar Abdelhamed [b], Ahmed Elaraby [c], Mahmoud Ahmed Mousa [d]

Show more ⌄

☰ Outline | ⤙ Share 〞 Cite

Get rights and content ↗

Abstract

Polyaniline (PANI), and graphitic C_3N_4 (GCU) have a significant research consideration owing to their properties. Accordingly, in the current study, PANI, GCU, and their composite (PANI@GCU) are synthesized through aniline chemical polymerization in the presence of C_3N_4. Materials characterizations are done using X-ray diffraction (XRD), Scanning electron microscopy (SEM), and Fourier transform infrared (FT-IR). SEM images demonstrate that the PANI layers cover the surface of the GCU. Samples are studied through dielectric and electrochemical analysis. The electrical conductivity value shows a conductivity increment in the order: PANI@GCU>PANI>GCU. The PANI@GCU composite sample exhibits a bulk conductivity of 23 S/m at 10MHz frequency. It also has a 584F/g specific capacitance with 96.7% stability after 1000 cycles at 1 A/g. The results of PANI@GCU supercapcitance performance are supported with molecular modelling that shows the interaction between GCU and PANI through the elongation of C-N bond of PANI beside of GCU layer bending to create arc and arrow structure. The structure of PANI@GCU has a lower band gap (ΔE_{gap}) than PANI, and GCU separately which agrees with the enhancement of the conductivity of the composite than its constituent.

Graphical abstract
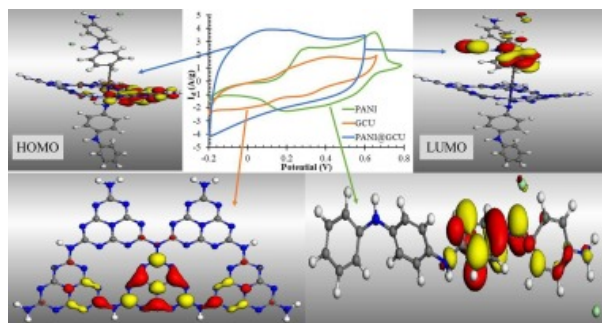
Download : Download high-res image (207KB)

Download : Download full-size image

Keywords

Conducting polymers; Dielectric; Graphitic carbon nitride; Composites; Supercapacitor

Introduction

Supercapacitors are energy storage devices that have generated a lot of interest due to their quick charging and discharging rates, high power density, and long lifespan [1]. Supercapacitors are ideal for a wide range of applications, such as regenerative braking systems in electric cars, backup power supplies, and portable electronics, thanks to these exceptional properties. The performance of the supercapacitor is mostly determined by the electrode material [2]. High-performance electrode materials are expected to have strong chemical stability to improve long-term cyclic reliability, a large specific surface area and appropriate porosity density to support the electrochemical reaction, and good electrical conductivity to improve the carrier's transport ability [2]. Recently, a lot of research has been done to find new materials that will work better as supercapacitor electrodes. Graphene and carbon nitride have garnered the most interest because of their large surface area and electrical solid conductivity.

g-C_3N_4 (Graphitic carbon nitride) (GCU) consists of C and N that are bound together as 2D conjugated polymer through sp^2 hybridization [3]. It exhibits the general formula $(C_3N_3H)_n$] and multiple allotropic phases with different band gaps, including a–C_3N_4 (5.49 eV), b–C_3N_4 (4.85 eV), cubic-C_3N_4 (4.3 eV), pseudo-C_3N_4 (4.13 eV), graphitic hexagonal triazine-C_3N_4 (2.97 eV), graphitic and hexagonal heptazine-C_3N_4 (0.93 eV) [4]. Due to its exceptional qualities, such as its low cost, vast surface area, earth-abundant nature, quick electron transfer, conjugation structure, lack of metal, and superior visible light-driven polymeric semiconductor, g-C_3N_4 has recently caught the attention of researchers [5]. Stability in hostile chemical environments solvents, thermal stability in air up to 600°C, biocompatibility, and catalytic properties [6]. Because of its high condensation degree and the presence of the heptazine ring structure, it also has excellent physicochemical stability and a unique electronic band structure. Due to structural defects and inadequate condensation, the –NH_2 functional groups contained around 2% H when the C/N molar ratio was 0.75 (the ideal value for g-C_3N_4) [5].

The g-C_3N_4 can be used for H_2 gas storage, CO_2 chelation and sensing, chelating and heavy metal remediation of polluted wastewater, catalysis [7], antifouling and bacterial coatings [8], and thermoelectric devices [9]. However, it is often inappropriate for electrochemical applications owing to integral low conductivity and surface area. Therefore, there are significant challenges to overcome the low conductivity before it can be used. This can be done by combining it with high-conducting materials such as polyaniline to form a composite [10].

g-C_3N_4 and its composites as electrode materials for eco-sustainable energy storage are still in the early stages compared to these highly researched sectors. That's why g-C_3N_4 composites can be used for various applications.

The term "composite design" refers to the process of combining several materials with diverse qualities. This technique has been used to improve the performance of many energy storage technologies. The electrochemical properties of g-C_3N_4 can be improved synergistically by utilising the advantages of both the pseudocapacitive phases of the added materials and g-C_3N_4. For example, bulk g-C_3N_4 has a relatively low specific capacitance of 81 F/g when tested at current densities of 0.5 A/g [11], whereas fabricated CoO and CuO decorated on g-C_3N_4 show a specific capacitance (CS) of 124.75 and 84.28 at 0.5 A/g, respectively [12]. At 10 mVs^{-1}, the capacitance of Gd decorated on g-C_3N_4 electrode was found to be 2.59 $mFcm^{-2}$ [13]. In 1 M Na_2SO_4, g-C_3N_4 and activated carbon displayed a specific capacitance value of 266 F/g [14]. At a current density of 1 A/g, g-C_3N_4 /PPy displayed a specific capacitance of 471 Fg^{-1} [15]. In addition, the capacitance of other composites, like $NiCo_2O_4$/O-g-C_3N_4 [16] with a current density of 1 A/g, Cu-g-C_3N_4 [17] with a current density of 0.5 Ag^{-1}, g-C_3N_4 /AgI [18] with a current density of 1.5 A/g, and MnO_2/g-C_3N_4 [19] with a capacitance of 87.6 F/g at the current density of 0.5 Ag^{-1} are also noteworthy. These studies demonstrate the potential of g-C_3N_4 binary materials as binary composites and their significance as supercapacitor electrode materials. For supercapacitor applications, materials comprising semiconductor oxides and g-C_3N_4 may perform better than either material alone.

Although several electrochemical studies have covered the majority of carbon nitride uses in great detail, GCU as an energy storage electrode has mostly been disregarded or is only briefly discussed earlier. That is why examining C_3N_4 use in supercapacitors may pave the way for future developments in this area [6], [7].

Polyaniline (PANI) is a conducting polymer that is widely utilised for electrode materials because of its outstanding conductivity and electrochemical properties; nevertheless, its low stability during charging and discharging cycles limits its development and uses. Graphitic carbon nitride (g-C_3N_4) was successfully added to the binary PANI/graphitic carbon nitride composite in order to solve these issues. Then, by taking into consideration the special qualities of the N heteroatomic ring structure of C_3N_4 and the adaptability of polyaniline conducting polymer, the composite was used as a supercapacitor. Van der Waals force restacking single-layered g-C_3N_4 results in low specific power and energy density; this can be easily avoided by linking g-C3N4 with PANI [17].

Low specific power and energy density may rise from the coupling of g-C3N4 with PANI, which may effectively impede the restacking of the single-layered g-C_3N_4 due to the Van der Waals force [17]. More pseudo-capacitance can be contributed more simply because of PANI's pseudo-capacitance property and the N-rich polymeric g-C_3N_4 framework, which provides more energetic reaction sites for electron donors and acceptors [10]. In light of the remarkable qualities of C_3N_4's N heteroatomic ring structure and the versatility of polyaniline conducting polymer, this work was created to describe the full-organic composite composed of C3N4 and PANI and its application as a supercapacitor. The newly created composite outperformed C_3N_4 bare electrodes and PANI in terms of cyclability and capacitance value. This study was supported by a theoretical study to show the interaction between PANI and C_3N_4 to explain the change in structure and the enhancement in dielectric and electrochemical performance.

Experimental

Preparation of C_3N_4 (GCU)

Based on the method mentioned in [21], g-C_3N_4 was synthesized through thermal decomposition of urea at 500 °C (5 °C/min) for 120 min.

Preparation of polyaniline (PANI)

Polyaniline was set with various adjustments to the previously mentioned methods [22]. 0.2 g of $BaCl_2 \cdot 6H_2O$ and 4 ml of monomer (aniline) were added to 400 ml of 1 M HCl. 0.1 L of 0.2 M $K_2S_2O_8$ was carefully added to this solution and

stirred continuously for 2 h at 5°C. After 1 day of holding to complete polymerization, the solution was washed with 0.25 L of deionized H_2O to remove contaminants. Eventually, the powder was dried at 60°C.

Preparation of PANI@GCU

PANI@GCU composite was synthesized with some modifications to the methodology cited [22]. 1 g of the prepared GCU was sonicated with 0.2 g of $BaCl_2 \cdot 6H_2O$ and aniline monomer with the mass ratio between GCU and aniline monomer 1:1, followed by the previous procedure PANI preparation.

Materials characterizations and measurements

XRD were captured using Cu-K with λ=1.54Å and 15° to 80° range using a Philips XL 40 X-ray diffractometer. (SEM/EDX/EDX mapping) (JEOL-JSM-6510 LV) was used to examine the materials' morphology and surface elemental analyses. BET was performed using Altamira Instruments, Inc. using N_2 at 77 K.

Electrical conductivity measurements were performed using a two-probe technique on pellets (r=0.65 mm and thickness=1 mm) generated by crushing powder at a pressure of 10^3 kg/cm^2. Pellets were covered with Ag paste to demonstrate the sample's ohmic contact. Ac-electrical measurements were obtained at 30°C using an LCR meter bridge (model HP 4284 A) at a constant voltage of 1 V and a frequency range of 10^3 to 10^7 Hz. The ε ' and ε″ values were estimated using Eqs. (1), (2) [23]

$$\varepsilon' = \frac{C\,t}{\varepsilon^o\,A_s} \tag{1}$$

$$\varepsilon''(\omega) = \varepsilon'(\omega)\tan\delta \tag{2}$$

where ε^o is space permittivity (8.86×10^{-12} F/m), t is thickness, A_s is the cross-sectional area of the pellet, and tan δ is a dissipative factor.

The electrochemical impedance spectroscopy (EIS), cyclic voltammetry (CV), and galvanostatic charge–discharge (GCD) techniques were utilized to calculate the energy storage capacity of the examined electrodes using the Netherlands' Metrohm Auto Lab PGSTAT 204. The electrochemical experiments were carried out using the standard three-electrode approach. The working electrodes were made by producing a paste comprising the components under research, acetylene black, PVF, and ethanol, coating it on FTO glass with a doctor blade approach, and drying it for two hours at 90°C. The Ag/AgCl electrode, Pt foil, and 0.2 M $LiClO_4$ aqueous solution were used to make the reference and counter electrodes.

Results and discussions

Characterizations

Fig. 1.a displays XRD of GCU, PANI, and PANI@GCU. GCU sample exhibits diffraction peaks at 12.8° and 27.6°, which are assigned to heptazine C_3N_4 and correspond to the (100) and (002) planes of hexagonal crystal. The conjugated aromatic rings' interplanar stacking peak is connected to the (002) crystal plane [24].
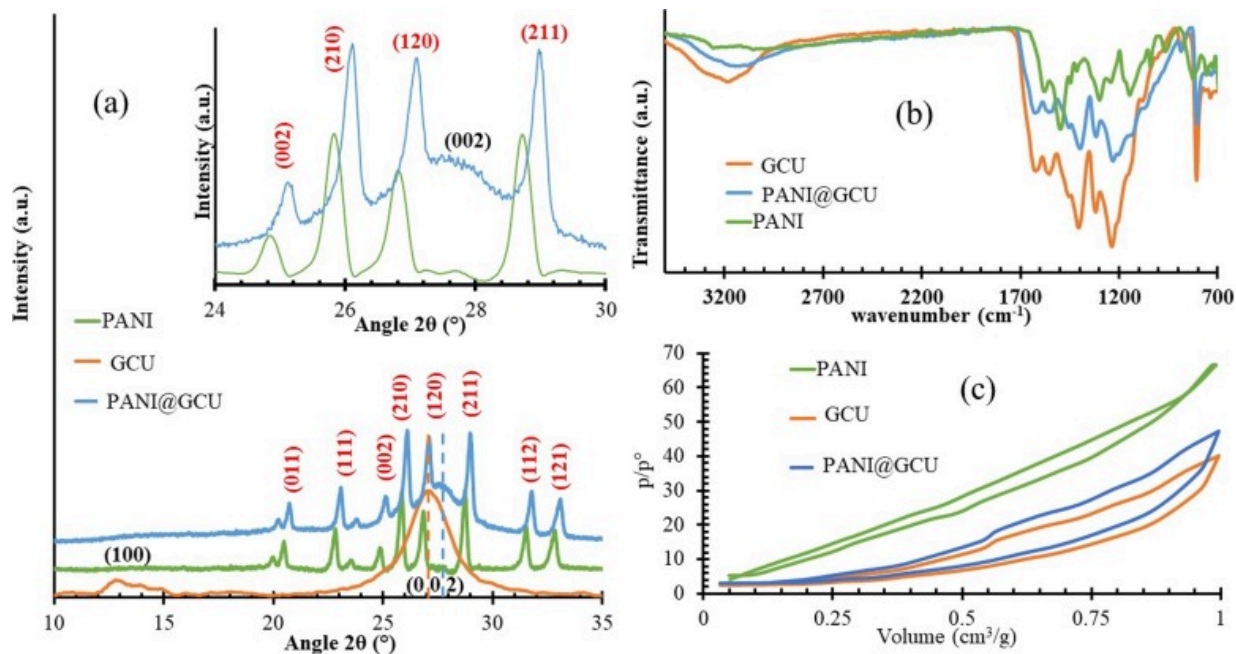
Download : Download high-res image (437KB)

Download : Download full-size image

Fig. 1. a) XRD, b) FT-IR, c) BET of the prepared materials.

XRD of PANI Fig. 1.a, shows the $BaSO_4$'s orthorhombic phase structure with referring to the (020), (111), (200), (021), (210), (121), (211), (002), (221), (022), (122), (140), (212), (041), and (330) plans, peaks at 20.3°, 22.8°, 23.9°, 25.6°, 26.8°, 28.6°, 31.7°, 32.8°, 36.1°, 38.5°, 39.8°, 42.5°, 42.8°, 43.8°, and 44.9°, respectively, (JCPDS card35-0782) [25]. The $BaSO_4$ is formed during the polymerization process through this equation

The fact that polyaniline crystallizes in orthorhombic phase form through assembling on the crystallite surfaces of $BaSO_4$ can be explained by the fact that PANI has many crystallite forms, which are orthorhombic structures similar to that of $BaSO_4$ [26], [27], [28], [29].

The observed XRD peaks for PANI and CCU in PANI@GCU sample are shifted than those obtained for pure PANI and GCU as seen in the inset Fig. 1a. This is due to the broken inter-layer hydrogen bonds, and the thinner g-C_3N_4 nanosheets, which are responsible for the moderate rise in diffraction peak, indicating that the c-spacing in PANI@GCU has significantly increased, as seen in Table 1.

Table 1. XRD and surface data of the prepared samples.

Sample	SSA (m²/g)	V_r (nm)	Scherer Debye			Lattice Parameter			
			D (nm)	δ (line/m²)	ε (×10⁻³)	a (Å)	b (Å)	c (Å)	V (Å³)
PANI	77.4	1.53	39.6	6.37×10¹⁴	1.91	7.151	8.69	5.434	337.68
GCU	80.3	1.44	3.7	7.3×10¹⁶	11.03	9.1	9.1	6.58	1415.6
PANI@GCU	88.6	1.39	37	7.27×10¹⁴	6.7	7.155	8.63	5.481	338.44
			2.82 *	1.2×10¹⁷ *	14.16 *	9.12*	9.12*	6.4*	1383*

*

Data from GCU peaks.

The lattice parameters of PANI, GCU, and PANI@GCU were estimated from XRD for hexagonal, and orthorhombic structures by using Eqs. (3), (4), respectively [30] and listed in Table 1.

$$dhkl = \sqrt{\frac{3}{4}\left(\frac{a^2}{h^2+hk+k^2}\right)} + \sqrt{\frac{c^2}{l^2}} \tag{3}$$

$$dhkl = \sqrt{\frac{a^2}{h^2}} + \sqrt{\frac{b^2}{k^2}} + \sqrt{\frac{c^2}{l^2}} \tag{4}$$

($h\ k\ l$) are Miller indices, and (a), (b), and (c) are the lattice constants. The crystallite size (D), and the strain (ε) of the investigated samples were calculated by Eqs. (5), (6), respectively [31], and listed also in Table 1.

$$D = \frac{0.9\lambda}{\beta\cos\theta} \tag{5}$$

$$\varepsilon = \frac{\beta}{4\tan\theta} \tag{6}$$

where λ=1.54Å used and β is FWHM of diffraction peak.

As seen in Table 1, addition of PANI on GCU leads to increased strain on GCU that leads to decreased c-space of PANI@GCU rather than GCU owing to PANI stacking on GCU graphitic layers that cause bending of layers.

Fig. 1.b shows the FT-IR PANI. Bands at 1553 cm^{-1} for C=C and 1470 cm^{-1} for C=N bond, proving the existence of pernigraniline form of PANI. Bands at 1287 cm^{-1} for N–H bending and 1235 cm^{-1} for C–N benzenoid ring stretching, indicate ermeraldiene salt presence. Additionally, band at 1038 cm^{-1} is linked to quinolinic-type ring-bending vibrational modes, which are connected to PANI formation [32].

FTIR spectra of GCU and its composite present in Fig. 1.b suggest the presence of the s-heptazine ring due to the appearance of bending vibrations at 807 cm^{-1}. The vibration bands noted at 1143–1629 cm^{-1} are related to aromatic C=N and C–N heterocycles stretching vibration [33]. The observed peaks at 1234 and 1553 cm^{-1} are related to the polymerization degree in C_3N_4 structures, and the noted band at 3168 cm^{-1} refers to –NH$_2$ in g-C_3N_4 [34].

N_2 adsorption/desorption isotherm is investigated and displayed in Fig. 1.c for a deeper understanding of surface properties. PANI, GCU, and PANI@GCU samples' isotherms were categorized as typical type IV [35], demonstrating the materials' mesoporous nature. The isotherm type is unaffected by PANI addition, although variations in surface characteristics like pore volume (V_p) and specific surface area (SSA) do occur. Table 1 provides a list of surface properties.

Fig. 2 shows the SEM and EDX images of the prepared samples. The SEM-micrograph of PANI shows agglomerated deformed spherical particles. In contrast, the image of GCU demonstrates small, hollow, irregular shapes that are strongly agglomerated in the order of ~10μm to ~30μm. The SEM image of the PANI@GCU shows distinctive morphology with white crystals of PANI covering the GCU surface. This morphology improves the surface, aiding the diffusion of the charges from the electrolyte into the bulk of the GCU [20]. The PANI@GCU composite shows the same morphology of its constituents with a uniform blend owing to the chemical methodology of preparation [36].
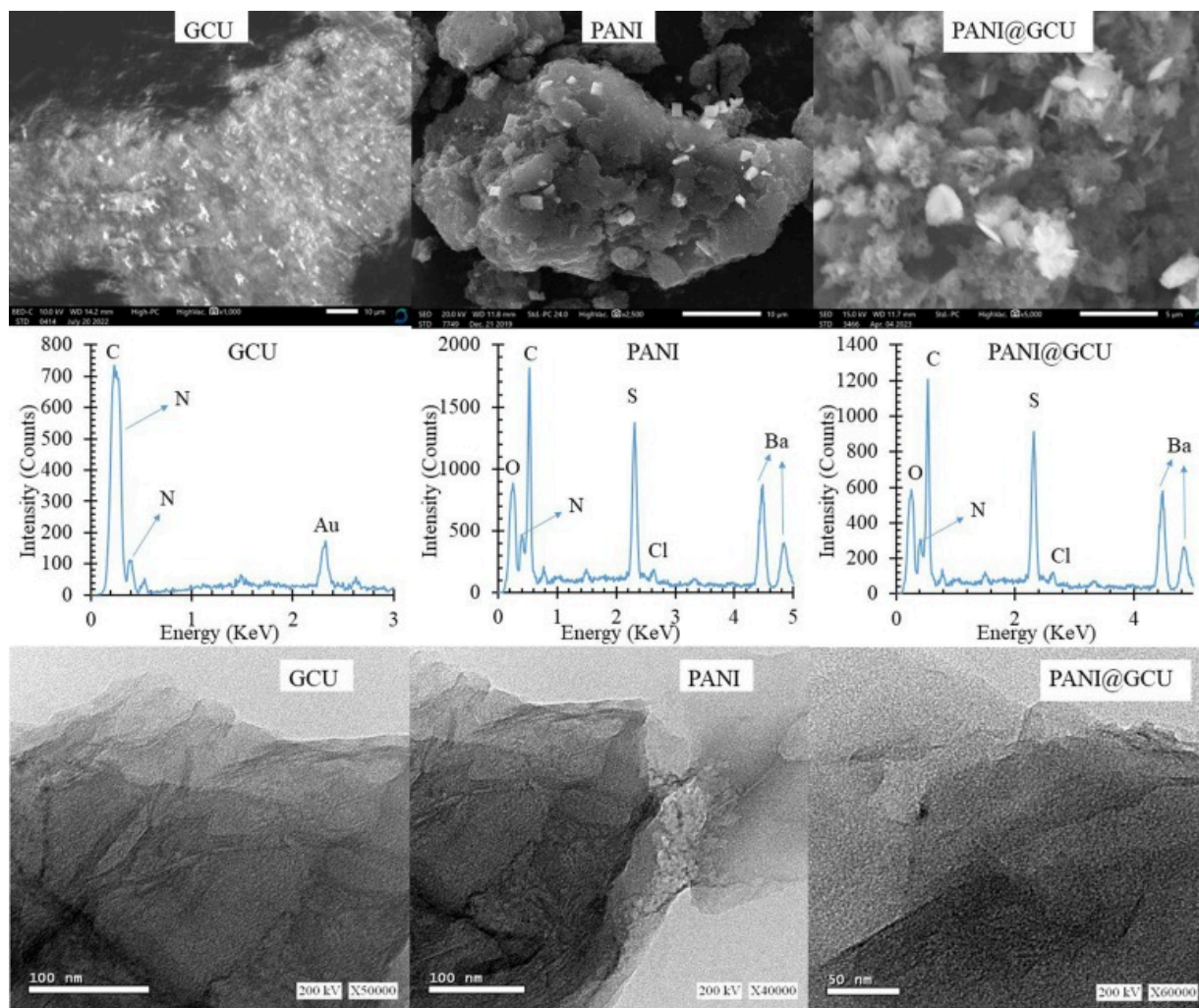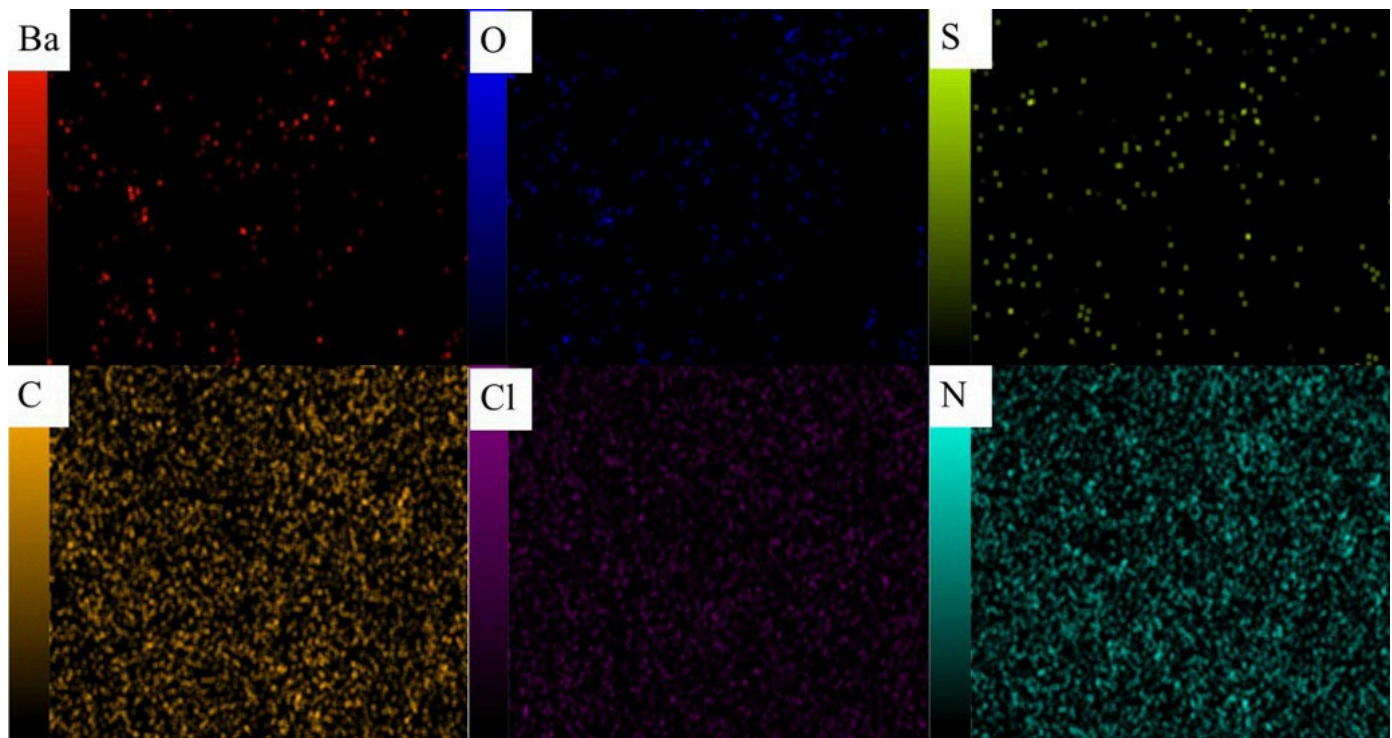
Fig. 2. SEM, EDX, and TEM of the prepared samples.

The EDX analysis confirms the elements contained in the produced samples. The results are shown in Fig. 3, and Table 2.

Fig. 3. EDX mapping of PANI@GCU.

Table 2. Elemental analysis of the prepared materials.

Sample	SEM-EDX (%)					
	C	N	Ba	S	O	Cl
PANI	73.1±1.9	21.4±2.1	1.0±0.2	1.0±0.2	1.7±0.3	1.8±0.3
GCU	36.3±1.5	62.5±2.6	—	—	—	—
PANI@GCU	45.2±3.8	53.5±1.8	0.8±0.1	0.7±0.1	0.7±0.2	0.9±0.3

TEM analysis was performed on the prepared samples to clarify the sheet structure that was obtained for them, as shown in Fig. 3. The presence of $BaSO_4$ doesn't affect on both morphologies of PANI or the binary composite.

Electrical studies

PANI, GCU, and PANI@GCU samples' dielectric behavior (dielectric loss, dielectric constant, impedance, and ac-conductivity) were examined at 30°C in frequencies between 10^3 and 10^7 Hz.

The dielectric constant (ε') is calculated using Eq. (1) and the results are represented in Fig. 4.(e and f). Materials showed a dielectric dispersion, where both ε' and ε'' values dropped rapidly as frequency rose in low-frequency range and nearly reached a frequency-independent behavior at higher frequencies [37]. The dielectric constant values at lower frequencies, both for PANI and its composites, lie in the range of $>10^8$ thus making it able to be categorized as a material with a high permittivity (high-k) [38]. The dielectric constant of PANI is lowered in the presence of g-C_3N_4. A Maxwell-Wagner-type relaxation caused by space charge release is indicated by the dielectric constant's sudden reduction with increasing frequency. This relaxation creates a high impedance barrier at the sample electrode

interface, which raises the dielectric constant's value. The dielectric constant (ε') falls and becomes frequency-independent in a high-frequency region as the applied electric field's frequency increases because the dipoles are unable to follow the applied field [39].
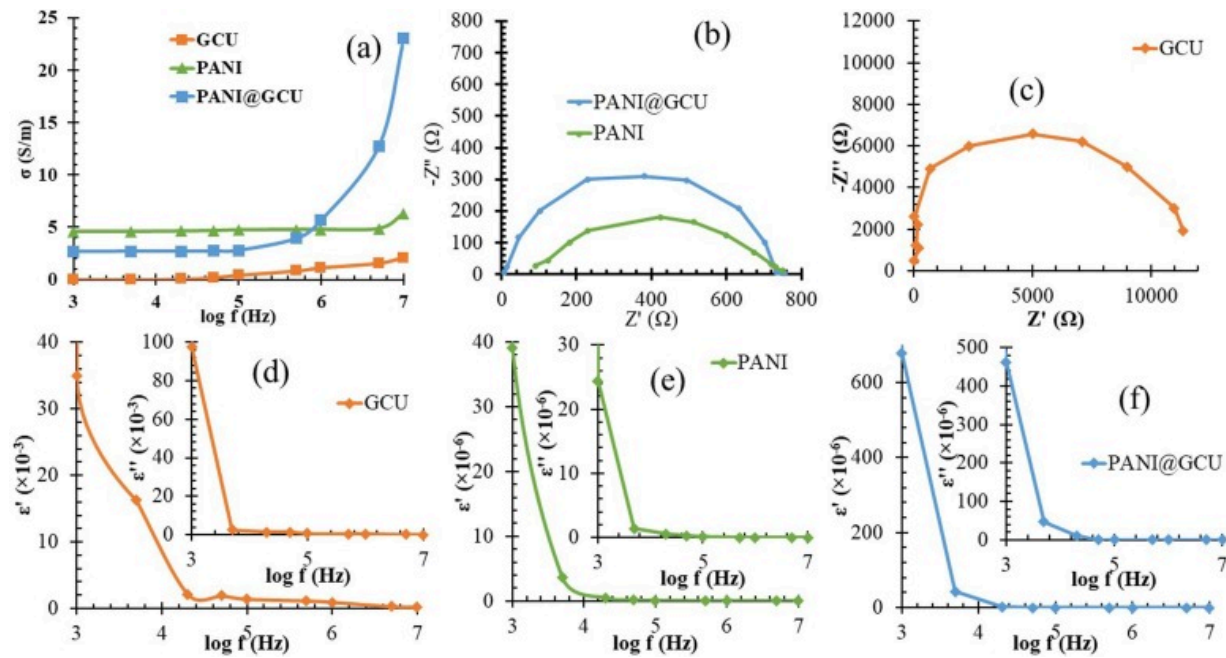
Download : Download high-res image (402KB)

Download : Download full-size image

Fig. 4. a) σ_{AC}, b and c) Cole-Cole diagram, d–f) ε', ε'' of the prepared materials.

Energy dissipation (ε'') in dielectrics can be explained in the form of tan δ or dielectric loss (ε'') which can be calculated by using Eq. (2) and the outcomes (ε'' vs. frequency) are also represented in Fig. 4.(e and f). The outcomes are equivalent to those found for the dielectric constant, which exhibits frequency-independent behavior at higher frequencies, nearly constant levels of maximum dispersion, and greatest dielectric loss at lower frequencies. The excess charge cannot diffuse along the field's direction due to the electric field's fast periodic reversal. Tangent loss is decreased as a result of the charges accumulating less. The dielectric loss of the PANI@g-C_3N_4 is greater than that of g-C_3N_4 at every measurement frequency. This explains why PANI sheets can generate electric current and partially convert electrical energy into heat energy when an electric field is applied to the dielectric g-C_3N_4. Additionally, PANI sheets are interconnected to create conducting channels that are well-aligned, which increases leakage current and dielectric loss [40].

The ac-conductivity (σ_{ac}) trend is studied using dielectric values according to Eq. (7) [40] and the results are represented in Fig. 4.a and summarized in Table 3.

$$\sigma_{ac}(\omega) = \varepsilon_0 \, \omega \, \varepsilon'' \tag{7}$$

Table 3. Ac-electrical properties data of the investigated materials.

Sample	1000Hz				500kHz				10MHz				
	σ (S/m)	ε'	ε''	tan δ	σ (S/m)	ε'	ε''	tan δ	σ (S/m)	ε'	ε''	tan δ	R_b (kΩ)
PANI	4.5	39×10^6	24.4×10^6	0.625	5.7	1.8×10^4	1.4×10^4	0.77	6.3	4510	4560	1.01	0.64
GCU	0.003	34×10^3	97×10^3	2.85	0.03	1.1×10^3	364.5	0.33	0.27	219	24.9	0.11	13.68

Sample	1000Hz				500kHz				10MHz				
	σ (S/m)	ε'	ε''	tan δ	σ (S/m)	ε'	ε''	tan δ	σ (S/m)	ε'	ε''	tan δ	R_b (kΩ)
PANI@GCU	2.7	6.7×10^8	8.6×10^8	1.28	5.7	14.8×10^3	6.4×10^3	0.43	24.9	5000	320	0.064	0.79

Results show σ_{ac} of g-C$_3$N$_4$ increases with the introduction of PANI as a result of creating conducting pathways in the PANI@g-C$_3$N$_4$ composite. Enhanced ε'' of the composite may also be caused due to improved conductivity. It is also worthwhile to mention that at low frequencies (up to 500kHz), the conductivity is more or less constant, and at higher frequencies there is a variation in conductivity. It is inferred that the composite has different AC conductivity at various frequencies.

EIS spectroscopy was used to further analyze the electrical characteristics of the samples under investigation. A Nyquist plot (Fig. 4.b and c) that illustrates the real (Z') and imaginary (Z'') components of impedance graphically represents the effects of grains, grain borders, and conduction processes. For every sample, there was just one semicircle visible. This indicates that there is just one relaxation time constant (t) for the polarisation of these materials. The relationship between the sample's resistance and arc radius is linear. At lower frequencies, the intercept of the semicircle with the Z' axis was used to calculate the bulk resistance R$_b$ [39]. Table 3 provides a summary of the EIS data that were gathered for the materials. This illustrates how the bulk resistance R$_b$ rises as indicated below

g-C$_3$N$_4$>PANI@g-C$_3$N$_4$>PANI

Electrochemical studies

Electrochemical techniques can be utilized to evaluate the material's suitability for energy storage applications to comprehend the storage mechanism and characteristics [41]. Therefore, the electrochemical behaviour of the prepared samples was studied using CV as a good tool for displaying various capacitive mechanisms kinds [42], [43]. The CV of the prepared electrodes was investigated at scan rates of 100, 50, 20, and 10mV/s are shown in Fig. S.1. The CV plot of GCU, Fig. 5.a, typically shows 2 redox points at 0.18V, and 0.4V, that related to the oxidation of the nitrogen atoms in C=N, and Li intercalation in either heptazine structure or c-space in GCU [44], [45].
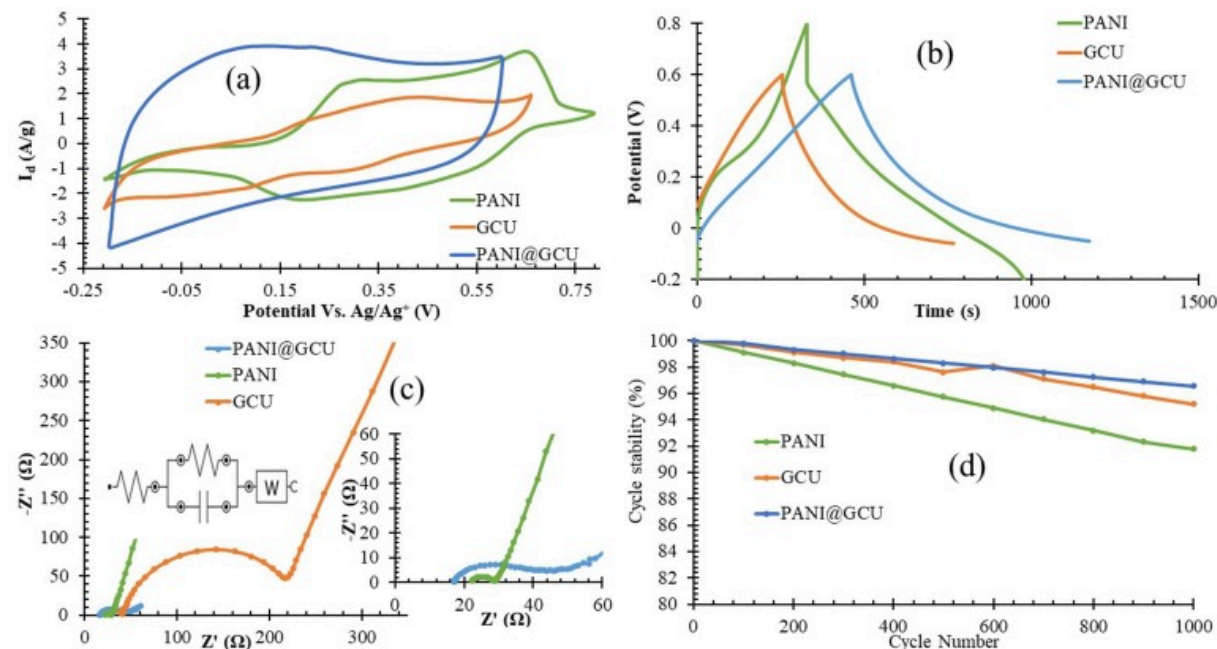
Download : Download high-res image (391KB)

Download : Download full-size image

Fig. 5. Electrochemical studies using a) CV at 10 mV/s, b) GCD at 1 A/g, c) Nyquist plot, d) cycling stability of the prepared materials.

The CV of PANI displayed 2 redox peaks at 0.49 V and 0.19 V due to the PRG↔ES↔LES reduction process. Moreover, other oxidation peaks appeared at 0.3 V and 0.64 V owing to LES↔ES↔PRG conversions, respectively [21], [46]. However, the CV of PANI@GCU shows a surface redox pseudocapacitive behavior owing to the good blending between the intercalation behavior [47], as shown in Fig. 5.a.

Using Eq. (8), the specific capacitance (C_{sp}) values of all the electrodes under investigation were calculated from CV plots [48], and given in Table 4

$$C_{sp} = \frac{1}{m\nu\Delta V} \int_{-V}^{+V} IV\partial V \tag{8}$$

where I is current, ΔV is applied potential, ν is scan rate, and m is the active material's mass.

Table 4. Electrochemical capacitive data of the investigated materials.

Sample	C_{sp} (F/g) 10mV/s	C_{sp} (F/g) 1 A/g	At 0.3V			Stability 1000 cycles (%)	E_d (Wh/g)	P_d (W/kg)	σ (mS/cm^2)	p	τ (ms)	R_S (Ω)	R_{ct} (Ω)
			b	k_1 (mA)	k_2 (mA)								
PANI	340.5	328.3	0.81	1.4	0.04	91.8	55.59	4103.7	24	0.88	0.015	22	6.7
GCU	375.6	365.2	0.72	0.8	0.05	95.2	540.72	4565	1.8	0.78	0.5	39	195
PANI@GCU	584	546.1	0.7	2.4	0.08	96.7	75.84	6067.7	11	0.65	0.3	17	29

For further analysis of capacitive behavior, b_o was determined through power law using Eq. (9) [49].

$$I_m = a \nu^{bo} \tag{9}$$

where I_m is the highest current density in CV plots, and a and b_o are constant parameters. According to Eq. (8), if the b_o value is generally=1.0, it refers to surface capacitive. If b_o=0.5, it refers to diffusion-controlled redox reaction [50]. Results and diagrams are seen in Fig. 6, and listed in Table 4.

$$I(V) = k_1 \nu^{1/2} + k_2\nu \tag{10}$$

Fig. 6. I-scan rate relation for capacitive behavior of the prepared samples.

Solving for the values of k_1 and k_2 in Eq. (10) at specific potential shows the separation of the diffusion and capacitive currents, respectively. It's noticed from k_1, and k_2 values, as shown in Fig. 7 and listed in Table 4, that composite tends to be higher for both diffusive and capacitive currents [51]. This is attributed to the mixed behavior of EDLC, and pseudocapacitive mechanisms of its constituents [52].
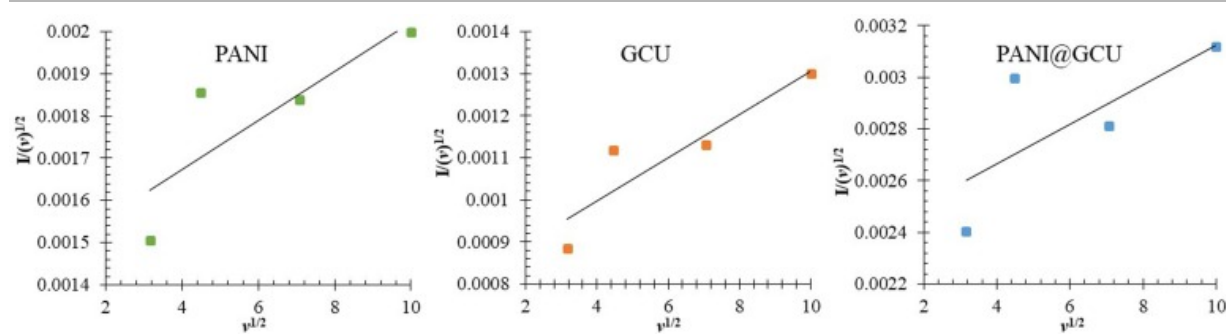
Download : Download high-res image (141KB)

Download : Download full-size image

Fig. 7. Capacitive and diffusive current of the prepared samples.

C_{sp} is better determined using the GCD technique. Thus, the GCD of all the samples was investigated at a current density of 1–5 A/g, and results are represented in Fig. S.2. At Fig. 7.b, all discharge curves show an internal resistance drop (IR-drop) that represents the equivalent series resistance (ESR) [53], [54] which is made up of all of the cell's resistances. The C_{sp} values were calculated from GCD using Eq. (11) [55] and the results are reported in Table 4

$$Csp = \frac{I\Delta t}{m\Delta V} \tag{11}$$

Δt is the discharge time and ΔV is the potential range during the charge–discharge measurement. The results show that the capacitance of the composite is higher than its constituents, as obtained from CV measurements [56]. This rise in capacitance is due to the higher SA and larger V_p of the composite which shorten the Li^+ path and speed up its diffusion [57]. The energy density (E_d) and power density (P_d) are important parameters. They are calculated for the prepared samples using Eqs. (12), 13), [57] and listed in Table 4

$$Ed = \frac{1}{2}C_{sp}\Delta V^2 \tag{12}$$

$$Pd = \frac{E_d}{t} \tag{13}$$

The electrochemical stability of the analyzed electrodes was also investigated at a current density of 1 A/g. The findings, represented in Fig. 7.d and summarised in Table 4, show that the electrodes' stability is slightly changed after 1000 cycles: 91.8, 95.2, and 96.7% of their initial capacitances for PANI, GCU, and PANI@GCU, respectively. The structural and morphological properties was almost the same after the discharging process as shown in Fig. S.3, that indicates the good stability of the prepared composite.

A basic understanding of ion diffusion, bulk electrolyte characteristics, electrode/electrolyte interface behavior, etc., is provided by EIS analysis [58], [59]. The charge-transfer resistance and low-frequency capacitance values in the various recorded frequency regions, as well as their influence on the supercapacitor cells' performance, were investigated using the EIS data [60], [61]. The impedance spectra (Nyquist plots across the 10^{-2}–10^5 Hz range) of every cell under study are displayed in Fig. 7.c. In the high-frequency domain, this corresponds to a semicircle, while in the low-frequency domain, it nearly forms a vertical line. Crossings of the $Z^/$ axis Nyquist diagram indicate the solution resistance (R_s) at higher frequencies [62], [63]. The diameter of the semicircle shows the charge transfer resistance (R_{ct}) at the electrode/electrolyte interface, which is connected to the surface property of the electrode [64], [65]. The spike at the

lower frequencies denotes the supercapacitance behavior of the samples and represents the diffusive resistance of Li^+ into samples [66]. The fitting data of the EIS spectra are listed in Table 4. From this, it is noted that the composite formation led to decreased R_{ct}, owing to an increment in c-space in GCU that increased Li^+ intercalation besides the behavior of PANI. The time constant (τ) of prepared electrodes was derived from the frequency (ω) coordinated at the maximum of semicircle using Eq. (14) [67]

$$\tau = \frac{1}{\omega} \qquad (14)$$

The results are listed in Table 4, which demonstrates that τ of GCU decreases due to introducing PANI.

For further confirmation of charge storage mechanism, we apply Eq. (15) [50]

$$Z = \frac{1}{B(i\omega)^p} \qquad (15)$$

where Z is the impedance, B is a constant, ω is the frequency, and p is a varied value. When p=1, this refers to capacitor behavior, and when p=0.5, this indicates semi-infinite diffusion of the battery. The results obtained are listed in Table 4, which is almost compatible with b_o calculated from CV data, which emphasizes and confirms the explanation of the high capacity of PANI@GCU composite. Table 6 shows a comparison result with different compounds compared with the prepared composite in this study.

Table 5. Quantum chemical parameters of the investigated compounds.

Compound	E_{HOMO} (eV)	E_{LUMO} (eV)	ΔE_{gap} (eV)	I (eV)	A (eV)
GCU	−0.171634	−0.111349	0.060285	0.171634	0.111349
PANI	−0.170064	−0.141472	0.028592	0.170064	0.141472
PANI@GCU	−0.156165	−0.137267	0.018898	0.156165	0.137267

Table 6. Comparison result of previous composite materials.

Composite	Cycle retention (%)	C_{sp}	Ref.
HKUST-1/PANI	87% (2000) cycles	270 F/g	[79]
PANI@CNF/CNS	98% (5000) cycles	308.8 F/g	[80]
PANI-FCC	84% (7000) cycles	135 F/g	[81]
PANI-PCNFs	74% (4500) cycles	165 F/g	[82]
PANI/CNT	86.8% (5000) cycles	180.7 mAh/g	[83]
PANI/carbon nanotube	92.7% (5000) cycles	3.96 F/cm^2	[84]
PANI / P&O C_3N_4	80% (500) cycles	294 F/g	[85]
PANI/ C_3N_4	86.2% (10000) cycles	234 F/g	[86]
PANI/ C_3N_4	96.7% (1000) cycles	584 F/g	This study

Theoretical modeling

Theoretical studies using DFT (Density Functional Theory) were used using the DMol3 module based on Generalised Gradient Approximation (GGA) and a Becke One Parameter (BOP) with fine quality tolerance parameters at BIOVIA

Materials Studio 6.0 software program and basic set Double Numerical plus Polarisation (DNP-3.5) to learn more about the reactivity and stability of the prepared samples, which verify the experimental results. The values of HOMO (Highest Occupied Molecular Orbital) and LUMO (Lowest Unoccupied Molecular Orbital), as well as the energy gap (ΔE_{gap}), electron affinity (A), and ionization potential (I), were used in this study to compute certain quantum chemical parameters. Fig. 8 depicts the optimized structures, HOMO-LUMO distributions, and electron density in the gas phase. The core orbitals HOMO (nucleophile centers) and LUMO (electrophile centers) [68], which represent the electron-sharing regions (donate and receive electrons) [69], are distributed over the chloride ion, quaternary N atoms, and benzene rings for the PANI compound and at alternate single and double bonds between N and C atoms for the GCU compound, respectively [70], [71]. The electron density (ED) cloud was shown to cover the entire geometry of the GCU and PANI compounds, reflecting the compounds' capacity for electron donation acceptance transfer [72]. PANI was optimized with the smallest unit of GCU (3 monomers), as can be seen in Fig. 9, to help with further prediction of the interaction between GCU and PANI in PANI@GCU. It was discovered that there were bores, which served as a little tunnel for PANI to pass through and communicate with other GCU layers. Additionally, the GCU geometry structure is famous for bending in a way that resembles an arc, which facilitates PANI transit. N-C bonds were found to be lengthened (bond length=7.656Å), which reduced steric resistance between GCU and PANI compound. This explains why the strain (ε) and dislocation density (δ) were reported to increase along with the change in the lattice parameters of the GCU (the "a" increment was caused by layer bending, while the "c" decrement was caused by layer bending and stacking to prevent steric hindrance). According to Fig. 8, Fig. 9, all the examined compounds have electron-sharing zones (donation-acceptance transfer) located over them [73]. This was further supported by the ED distribution. Based on HOMO and LUMO energy values, the stability and reactivity of the investigated compounds were determined using the following Eqs. [74].

$$I = -E_{\mathrm{HOMO}} \tag{16}$$

$$A = -E_{\mathrm{LUMO}} \tag{17}$$

$$\Delta E_{gap} = E_{LUMO} - E_{HOMO} \tag{18}$$
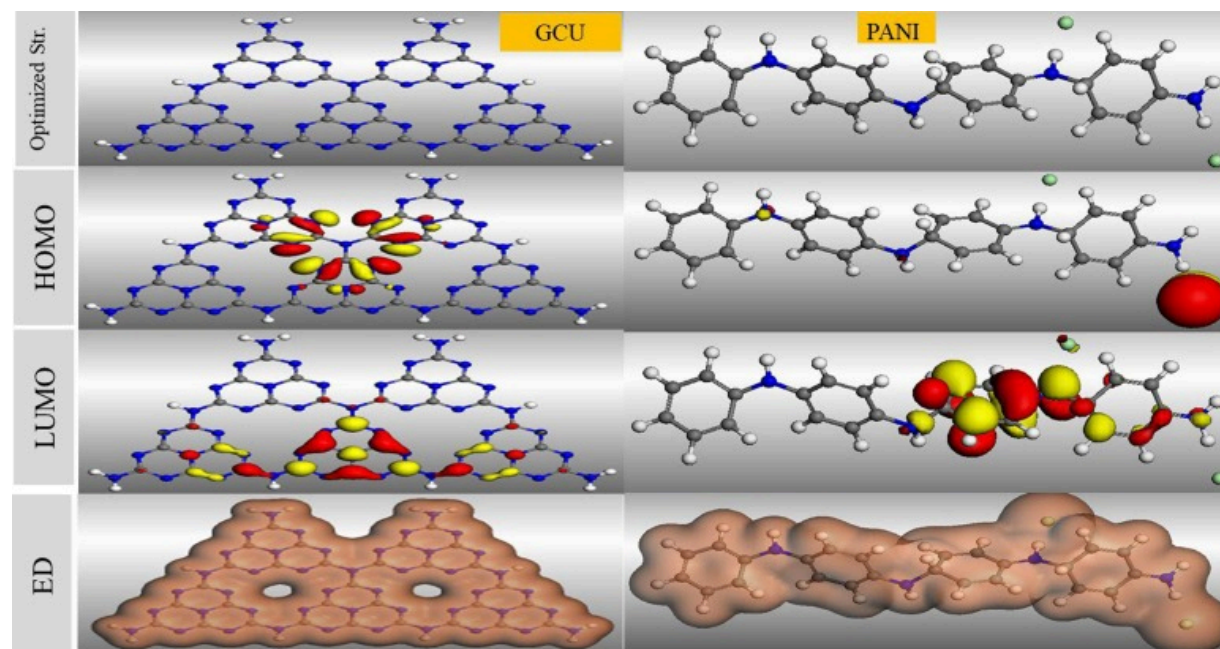
Fig. 8. The optimized structure, total electron density, HOMO and LUMO orbital occupation for PANI, and GCU.
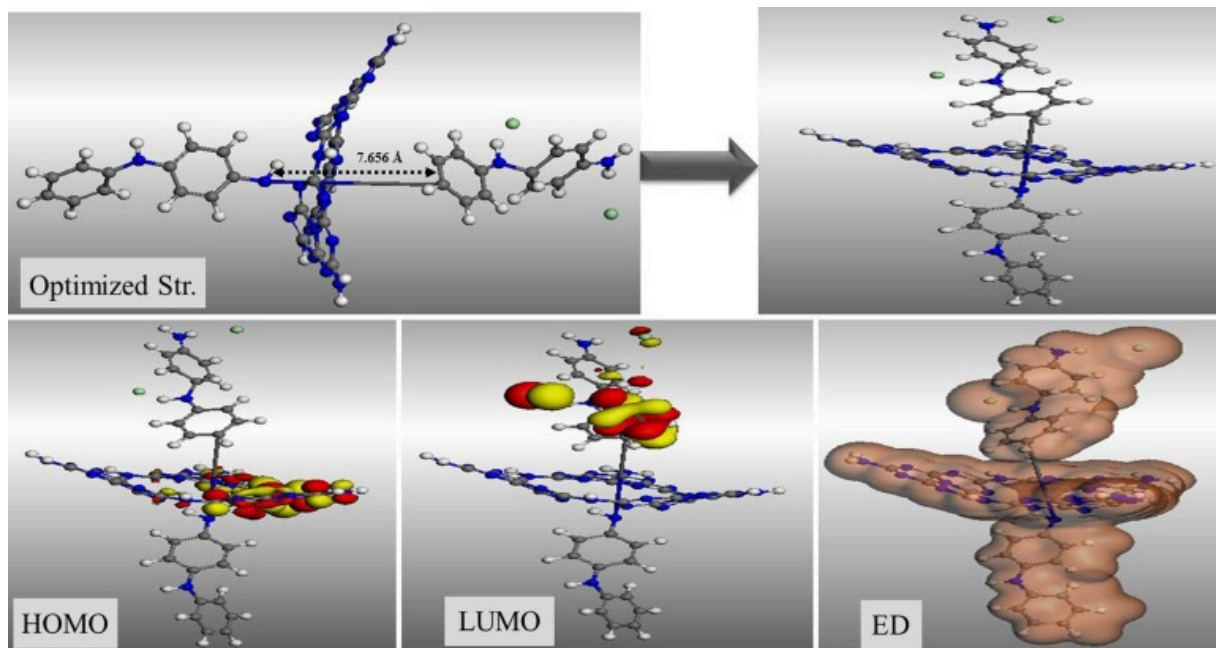
Fig. 9. The optimized structure, ED, HOMO and LUMO orbital occupation for the investigated PANI@GCU.

According to Table 5's HOMO value, PANI@GCU has a larger tendency to donate electrons than PANI and GCU compounds, with a value of −0.156 eV. At the same time, GCU compounds with a higher potential to collect electrons showed lower values of LUMO [75]. The ionization potential value can be used to explain the molecules' chemical reactivity [76]. Table 5's PANI@GCU with lower ionization energy values suggested that the atoms and molecules were more reactive than they were in PANI and GCU [77]. PANI@GCU has a lower energy gap value than PANI and GCU, according to Table 5. This finding demonstrates that PANI@GCU has significant conduction due to the geometry of its structure. As a result, when its conductivity rises, ΔE_{gap} is reduced [78], which explains the higher value of AC conductivity and electrochemical performance of PANI@GCU composite.

Conclusions

This research investigated how PANI affected the physicochemical properties of C_3N_4 through the formation of PANI@GCU nanocomposites. First, PANI and composite were created through chemical polymerization, then composite was created through the polymerization of an aniline monomer with the presence of GCU. By analyzing the synthesized materials using FT-IR, XRD, BET, SEM, and EDX, it was confirmed that polymer and GCU were present in the nanocomposites. The PANI@GCU nanocomposite demonstrates a striking electrochemical performance, electrical conductivity, and dielectric properties, enhancement as a result of the synergistic effects between PANI and GCU. The produced samples are appropriate for high-frequency applications in electrical circuits to reduce dielectric losses because of the composite's low values of dielectric loss at high frequencies. These prepared samples are also appropriate for high-frequency applications to reduce eddy currents due to their higher electrical resistivity. PANI@GCU composite has a high C_{sp} (546 F/g) with a high stability of 96.7% from its original capacitance after 1000 cycles. The Theoretical modeling shows the interaction between PANI and GCU that shows the change in C-N bond length in PANI beside the GCU layer bending like an arc to avoid the steric hindrance. The new molecular structure can explain the structural, electrical, and electrochemical behaviour of the PANI@GCU composite.

CRediT authorship contribution statement

Khaled Faisal Qasim: Writing – original draft, Methodology, Investigation, Conceptualization. **Samar Abdelhamid:** Validation, Data curation. **Ahmed Elaraby:** Writing – original draft, Validation, Software, Formal analysis. **Mahmoud Ahmed Mousa:** Writing – review & editing, Supervision, Project administration.

Declaration of competing interest

The authors declare that they have no known competing financial interests or personal relationships that could have appeared to influence the work reported in this paper.

Appendix A. Supplementary data

The following are the Supplementary data to this article:

📄 Download : Download Word document (439KB)

Supplementary Data 1.

Recommended articles

References

[1] S. Rajagopal, R.P. Vallikkattil, M.M. Ibrahim, D.G. Velev
Condens. Matter, 7 (2022), p. 6

CrossRef ↗   Google Scholar ↗

[2] Z.S. Iro, C. Subramani, S.S. Dash
Int. J. Electrochem. Sci., 11 (2016), pp. 10628-10643, 10.20964/2016.12.50 ↗
📄 View PDF   View article   View in Scopus ↗   Google Scholar ↗

[3] F. Magesa, *et al.*
Trends Environ. Anal. Chem., 23 (2019), p. e00064
📄 View PDF   View article   View in Scopus ↗   Google Scholar ↗

[4] Q. Hao, et al., Nano Res. 12(1) (2019).
Google Scholar ↗

[5] H. Xiao, Z.P. Zhang, Z.X. Huang, M.Z. Rong, M.Q. Zhang
Compos. Commun., 23 (November) (2021), Article 100584, 10.1016/j.coco.2020.100584 ↗
📄 View PDF   View article   View in Scopus ↗   Google Scholar ↗

[6] X. Li, *et al.*
Compos. Commun., 23 (2020), Article 100578, 10.1016/j.coco.2020.100578 ↗
View in Scopus ↗   Google Scholar ↗

[7] F.-Y. Liu, H.-Y. Zeng, J. Xiong, D.-Y. Peng, S. Xu, D.-S. An
New J. Chem., 46 (2022), pp. 15937-15949, 10.1039/d2nj02162e ↗
View in Scopus ↗   Google Scholar ↗

[8] J. Hou, S. Liu, X. Jiang, G.I.N. Waterhouse, Z. Zhang, L. Yu
Prog. Org. Coat., 154 (February) (2021), Article 106203, 10.1016/j.porgcoat.2021.106203 ↗

View PDF   View article   View in Scopus ↗   Google Scholar ↗

[9]   V. Ugraskan, F. Karaman

J. Electron. Mater., 50 (2021), pp. 3455-3461, 10.1007/s11664-021-08856-1 ↗

View in Scopus ↗   Google Scholar ↗

[10]   M. Ghaemmaghami

Sustain. Energy Fuels, 3 (2019), pp. 2176-2204, 10.1039/c9se00313d ↗

View in Scopus ↗   Google Scholar ↗

[11]   M. Tahir, et al.

ACS Appl. Mater. Interfaces, 6 (2014), pp. 1258-1265

CrossRef ↗   View in Scopus ↗   Google Scholar ↗

[12]   R.S. Santos, R.S. Babu, M. Devendiran, D.B. Haddad, A.L.F. De Barros

Mater. Lett., 308 (September) (2022), Article 131156

View PDF   View article   View in Scopus ↗   Google Scholar ↗

[13]   S. Kumar, A. Ghorai, A. Midya, C. Sekhar, T. Kumar

Chem. Phys. Lett., 796 (December) (2022), Article 139572, 10.1016/j.cplett.2022.139572 ↗

Google Scholar ↗

[14]   S. Pilathottathil, J. Kavil, M. Shahin

Mater. Sci. Eng. B, 276 (November) (2022), Article 115573, 10.1016/j.mseb.2021.115573 ↗

View PDF   View article   View in Scopus ↗   Google Scholar ↗

[15]   G. Dong, H. Fan, K. Fu, S. Zhang, M. Zhang, W. Wang

Compos. Part B Eng., 162 (2019), pp. 369-377, 10.1016/j.compositesb.2018.12.098 ↗

View PDF   View article   View in Scopus ↗   Google Scholar ↗

[16]   S. Pany, A. Nashim, K. Parida, P.K. Nanda

ACS Appl. Nano Mater. Mater., 4 (2021), pp. 10173-10184

CrossRef ↗   View in Scopus ↗   Google Scholar ↗

[17]   S.Y. Dhar, I. Hussain, M. Devi, R. Dasgupta

IEEE Trans. Nanotechnol., 21 (2022), pp. 474-480

Google Scholar ↗

[18]   A. Meftahi, M. Shabani-nooshabadi, A. Reisi-vanani

Electrochim. Acta, 430 (January) (2022), Article 141052, 10.1016/j.electacta.2022.141052 ↗

View PDF   View article   View in Scopus ↗   Google Scholar ↗

[19]   H. Soltani, H. Bahiraei, S. Ghasemi

J. Alloys Compd., 904 (2022), Article 163565, 10.1016/j.jallcom.2021.163565 ↗

View PDF   View article   View in Scopus ↗   Google Scholar ↗

[20]   R. Gonçalves, R.S. Paiva, T.M. Lima, M.W. Paixão, E.C. Pereira, Electrochim. Acta (2020) 137570. doi: 10.1016/j.electacta.2020.137570.

Google Scholar ↗

[21]   B. Dong, et al.

ACS Appl. Mater. Interfaces, 9 (2017), pp. 17890-17896

CrossRef ↗   View in Scopus ↗   Google Scholar ↗

[22] K.F. Qasim, M.A. Mousa, J. Inorg. Organomet. Polym. Mater. (2023) (in press). doi: 10.1007/s10904-023-02720-x.

Google Scholar ↗

[23] K.F. Qasim, M.A. Mousa
Egypt. J. Pet., 30 (4) (2021), pp. 9-19, 10.1016/j.ejpe.2021.09.001 ↗

📄 View PDF   View article   View in Scopus ↗   Google Scholar ↗

[24] J. Li, Y. Wang, X. Li, Q. Gao, S. Zhang
J. Alloys Compd., 881 (2021), Article 160551, 10.1016/j.jallcom.2021.160551 ↗

📄 View PDF   View article   View in Scopus ↗   Google Scholar ↗

[25] Y. Shen, C. Li, X. Zhu, A. Xie, L. Qiu, J. Zhu
J. Chem. Sci., 119 (4) (2007), pp. 319-324

CrossRef ↗   Google Scholar ↗

[26] H. Wang, Q. Hao, X. Yang, L. Lu, X. Wang
Nanoscale, 2 (10) (2010), pp. 2164-2170, 10.1039/c0nr00224k ↗

View in Scopus ↗   Google Scholar ↗

[27] R. Gottam, P. Srinivasan
New J. Chem., 39 (11) (2015), pp. 8545-8551, 10.1039/c5nj01687h ↗

View in Scopus ↗   Google Scholar ↗

[28] Á.B. Sifontes, et al.
J. Nanomater., 2015 (2015), pp. 1-8

CrossRef ↗   Google Scholar ↗

[29] N. Mahato, N. Parveen, M.H. Cho
Mater. Lett., 161 (2015), pp. 372-374, 10.1016/j.matlet.2015.08.138 ↗

📄 View PDF   View article   View in Scopus ↗   Google Scholar ↗

[30] P. Gellings, H. Bouwmeester
The CRC Handbook of Solid State Electrochemistry
(first ed.), CRC Press (1997)

Google Scholar ↗

[31] N. Ahmed, M. Ramadan, W.M.A. El
Int. J. Hydrogen Energy, 43 (October) (2018), pp. 21219-21230, 10.1016/j.ijhydene.2018.10.012 ↗

📄 View PDF   View article   View in Scopus ↗   Google Scholar ↗

[32] V.J. Babu, S. Vempati, S. Ramakrishna
Mater. Sci. Appl., 4 (1) (2013), pp. 1-10, 10.4236/msa.2013.41001 ↗

Google Scholar ↗

[33] J. Zhu, P. Xiao, H. Li, S.A.C. Carabineiro
ACS Appl. Mater. Interfaces, 6 (19) (2014), pp. 16449-16465, 10.1021/am502925j ↗

View in Scopus ↗   Google Scholar ↗

[34]   H. Dai, *et al.*

Diam. Relat. Mater., 38 (2013), pp. 109-117, 10.1016/j.diamond.2013.06.012 ↗

🗎 View PDF   View article   View in Scopus ↗   Google Scholar ↗

[35]   S.K. Mohamed, A.M.A. Bashat, H.M.A. Hassan, N. Ismail, W.M.A. El Rouby

RSC Adv., 13 (20) (2023), pp. 14018-14032, 10.1039/d3ra02011h ↗

View in Scopus ↗   Google Scholar ↗

[36]   A. Alaghmandfard, K. Ghandi, 12(2) (2022). doi: 10.3390/nano12020294.

Google Scholar ↗

[37]   Y. Zheng, Z. Zhang, C. Li

J. Photochem. Photobiol. A Chem., 332 (2017), pp. 32-44, 10.1016/j.jphotochem.2016.08.005 ↗

🗎 View PDF   View article   View in Scopus ↗   Google Scholar ↗

[38]   C. Ho, C. Liu, C. Hsieh, K. Hsieh, S. Lee

Synth. Met., 158 (2008), pp. 630-637, 10.1016/j.synthmet.2008.04.014 ↗

🗎 View PDF   View article   View in Scopus ↗   Google Scholar ↗

[39]   A.S. Roy, S.G. Hegde, A. Parveen

Polym. Adv. Technol., 25 (1) (2014), pp. 130-135, 10.1002/pat.3214 ↗

View in Scopus ↗   Google Scholar ↗

[40]   M. Khairy, M.A. Mousa

Int. J. Mater. Chem., 2 (5) (2013), pp. 197-204, 10.5923/j.ijmc.20120205.03 ↗

Google Scholar ↗

[41]   H. M. A. Hassan, et al., Molecules 28(7) (2023). doi: 10.3390/molecules28073072.

Google Scholar ↗

[42]   B. Cao, *et al.*

J. Colloid Interface Sci., 661 (January) (2024), pp. 598-605, 10.1016/j.jcis.2024.01.201 ↗

🗎 View PDF   View article   View in Scopus ↗   Google Scholar ↗

[43]   H. Liu, *et al.*

Adv. Funct. Mater., 34 (2024), Article 2309840

View in Scopus ↗   Google Scholar ↗

[44]   Z.Y. Yang, *et al.*

ACS Appl. Mater. Interfaces, 6 (11) (2014), pp. 8497-8504, 10.1021/am501362g ↗

View in Scopus ↗   Google Scholar ↗

[45]   Z.G. Shiquan Hong, X. Huang, H. Liu

J. Inorg. Organomet. Polym. Mater., 29 (2019), pp. 1587-15960

Google Scholar ↗

[46]   F. Wang, M. Rafiee, S.S. Stahl

Z. Angew. Chem., 130 (2018), pp. 6796-6800, 10.1002/ange.201803539 ↗

Google Scholar ↗

[47]   L. Wang, *et al.*

Sci. Rep., 3 (2013), pp. 1-9, 10.1038/srep03568 ↗

📄 View PDF   View article   Google Scholar ↗

[48]   M. Ciszewski, A. Mianowski, P. Szatkowski, G. Nawrat, J. Adamek

Ionics (kiel), 21 (2) (2014), pp. 557-563, 10.1007/s11581-014-1182-4 ↗

Google Scholar ↗

[49]   S. Kalasina, *et al.*

Sci. Rep., 8 (1) (2018), pp. 1-11, 10.1038/s41598-018-30707-z ↗

Google Scholar ↗

[50]   A.E. Etman, A.M. Ibrahim, F.A.M. Darwish, K.F. Qasim

J. Ind. Eng. Chem., 122 (2023), pp. 27-45, 10.1016/j.jiec.2023.03.008 ↗

📄 View PDF   View article   View in Scopus ↗   Google Scholar ↗

[51]   Y. Shao, *et al.*

Chem. Rev., 118 (18) (2018), pp. 9233-9280, 10.1021/acs.chemrev.8b00252 ↗

View in Scopus ↗   Google Scholar ↗

[52]   S. Lindstrom Henrik, A. So, J. Solbrand, A.H. Hjelm, S. Lindquist

J. Phys. Chem. B, 2 (97) (1997), pp. 7717-7722

Google Scholar ↗

[53]   M. Khairy, W.A. Bayoumy, K. Faisal, E.E. Elshereafy, M.A. Mousa

J. Inorg. Organomet. Polym. Mater., 30 (8) (2020), pp. 3158-3169, 10.1007/s10904-020-01478-w ↗

View in Scopus ↗   Google Scholar ↗

[54]   R. Abazari, S. Sanati

Inorg. Chem., 8 (2022), pp. 3396-3405

CrossRef ↗   View in Scopus ↗   Google Scholar ↗

[55]   K.F. Qasim, W.A. Bayoumy, M.A. Mousa

J. Mater. Sci. Mater. Electron., 31 (2020), pp. 19526-19540, 10.1007/s10854-020-04482-5 ↗

View in Scopus ↗   Google Scholar ↗

[56]   S.K. Mohamed, S.A. Elsalam, A. Shahat, H.M.A. Hassan, R.M. Kamel

New J. Chem., 45 (4) (2021), pp. 1904-1914, 10.1039/d0nj05412g ↗

View in Scopus ↗   Google Scholar ↗

[57]   K.F. Qasim, M.A. Mousa

J. Inorg. Organomet. Polym. Mater., 32 (8) (2022), pp. 3093-3105, 10.1007/s10904-022-02335-8 ↗

View in Scopus ↗   Google Scholar ↗

[58]   S. Sanati, A. Morsali, H. García

J. Energy Chem., 87 (2023), pp. 540-567, 10.1016/j.jechem.2023.08.042 ↗

📄 View PDF   View article   View in Scopus ↗   Google Scholar ↗

[59]   S. Sanati, Q. Wang, R. Abazari, M. Liu

Chem. Commun., 60 (2024), pp. 3129-3137

View article   CrossRef ↗   View in Scopus ↗   Google Scholar ↗

[60]   H. Liu, L. Hu, R.A. Soomro, B. Xu

Chinese Chem. Lett., 34 (8) (2023), Article 108004, 10.1016/j.cclet.2022.108004 ↗

📄 View PDF   View article   View in Scopus ↗   Google Scholar ↗

[61]   H. Liu, et al., Adv. Energy Mater. (in press) (2024).

Google Scholar ↗

[62]   N.K. Sidhu, A.C. Rastogi

Synth. Met., 219 (2016), pp. 1-10, 10.1016/j.synthmet.2016.04.012 ↗

📄 View PDF   View article   View in Scopus ↗   Google Scholar ↗

[63]   K. Adams, J. Mallows, T. Li, D. Kampouris, J.H.J. Thijssen, N. Robertson, J. Phys. Energy (1)(3) (2019). doi: 10.1088/2515-7655/ab22d7.

Google Scholar ↗

[64]   R. Rajalakshmi, K.P. Remya, C. Viswanathan, N. Ponpandian

Nanoscale Adv., 3 (10) (2021), pp. 2887-2901, 10.1039/d1na00144b ↗

View article   View in Scopus ↗   Google Scholar ↗

[65]   S. Sanati, Z. Rezvani, B. Habiby

New J. Chem., 42 (2018), pp. 18426-18436, 10.1039/c8nj04402c ↗

View in Scopus ↗   Google Scholar ↗

[66]   E.A. Kamar, K.F. Qasim, M.A. Mousa

Electrochim. Acta, 430 (2022), Article 141106, 10.1016/j.electacta.2022.141106 ↗

📄 View PDF   View article   View in Scopus ↗   Google Scholar ↗

[67]   M. Wilkening, R. Amade, W. Iwaniak, P. Heitjans

Phys. Chem. Chem. Phys., 9 (10) (2007), pp. 1239-1246, 10.1039/b616269j ↗

View in Scopus ↗   Google Scholar ↗

[68]   R.A. El-nagar, A. Elaraby, M.I. Nessim, A. Ghanem, J. Mol. Liq. 401(March) (2024) 124708. doi: 10.1016/j.molliq.2024.124708.

Google Scholar ↗

[69]   A. Elaraby, et al., Colloids Surf. A (2022) 130687. doi: 10.1016/j.colsurfa.2022.130687.

Google Scholar ↗

[70]   N.M. El Basiony, *et al.*

J. Mol. Liq., 400 (October) (2024), Article 124475, 10.1016/j.molliq.2024.124475 ↗

📄 View PDF   View article   View in Scopus ↗   Google Scholar ↗

[71]   N.M. El Basiony, *et al.*

Mater. Today Commun., 37 (August) (2023), Article 107378, 10.1016/j.mtcomm.2023.107378 ↗

📄 View PDF   View article   View in Scopus ↗   Google Scholar ↗

[72]   A. Elaraby, K.F. Qasim, S.K. Mohamed, E.A. El-Sharkawy, S. Abdelhamed

J. Environ. Chem. Eng., 12 (1) (2024), Article 111861, 10.1016/j.jece.2023.111861 ↗

📄 View PDF   View article   View in Scopus ↗   Google Scholar ↗

[73]   A. Nasser, M.A. Migahed, N.M. EL Basiony, H.M. Abd-El-Bary, T.A. Mohamed
        Sci. Rep., 13 (1) (2023), pp. 1-17, 10.1038/s41598-023-37321-8 ↗

        Google Scholar ↗

[74]   N.M. El Basiony, E.E. Badr, S.A. Baker, A.S. El-Tabei
        Appl. Surf. Sci., 539 (October) (2021), Article 148246, 10.1016/j.apsusc.2020.148246 ↗
        🔒 View PDF   View article   View in Scopus ↗   Google Scholar ↗

[75]   E.A.M. Gad, E.M.S. Azzam, S.A. Halim
        Egypt. J. Pet., 27 (4) (2018), pp. 695-699, 10.1016/j.ejpe.2017.10.005 ↗
        🔒 View PDF   View article   View in Scopus ↗   Google Scholar ↗

[76]   A. Elaraby, S.A. El-samad, E.A. Khamis, E.G. Zaki
        Sci. Rep., 13 (1) (2023), pp. 1-18, 10.1038/s41598-023-27513-7 ↗

        Google Scholar ↗

[77]   T. Chakraborty, K. Gazi, D.C. Ghosh
        Mol. Phys., 108 (16) (2010), pp. 2081-2092, 10.1080/00268976.2010.505208 ↗
        View in Scopus ↗   Google Scholar ↗

[78]   M.A. Migahed, A. Nasser, H. Elfeky, M.M. El-Rabiei
        RSC Adv., 9 (46) (2019), pp. 27069-27082, 10.1039/c9ra04461b ↗
        View in Scopus ↗   Google Scholar ↗

[79]   E.A. Jafari, M. Moradi, S. Borhani, H. Bigdeli, S. Hajati
        Phys. E, 99 (January) (2018), pp. 16-23, 10.1016/j.physe.2018.01.007 ↗
        🔒 View PDF   View article   View in Scopus ↗   Google Scholar ↗

[80]   S. Liu, K. Wan, C. Zhang, T. Liu
        Compos. Commun., 24 (2021), 10.1016/j.coco.2020.100610 ↗

        Google Scholar ↗

[81]   M. Hashemi, M.S. Rahmanifar, M.F. El-Kady, A. Noori, M.F. Mousavi, R.B. Kaner
        Nano Energy, 44 (2018), pp. 489-498, 10.1016/j.nanoen.2017.11.058 ↗
        🔒 View PDF   View article   View in Scopus ↗   Google Scholar ↗

[82]   S.K. Simotwo, V. Kalra
        Electrochim. Acta, 268 (2018), pp. 131-138, 10.1016/j.electacta.2018.01.157 ↗
        🔒 View PDF   View article   View in Scopus ↗   Google Scholar ↗

[83]   J. Du, et al.
        J. Energy Storage, 33 (2021), 10.1016/j.est.2020.102165 ↗

        Google Scholar ↗

[84]   Y. Liu, Z. Qin, Y. Shen, Z. Dou, N. Liu
        Carbon N. Y., 186 (2022), pp. 688-698, 10.1016/j.carbon.2021.10.066 ↗
        🔒 View PDF   View article   View in Scopus ↗   Google Scholar ↗

[85]   M.E. Martínez-Cartagena, et al.
        Polymers (basel), 14 (2022), p. 3913

CrossRef ↗   View in Scopus ↗   Google Scholar ↗

[86]   X. Qin, J. Wan, Q. Zhang, Y. Zhang, H. Yu, S. Shi

Carbon Lett., 33 (2023), pp. 781-790

CrossRef ↗   View in Scopus ↗   Google Scholar ↗

Cited by (0)

[View Abstract](#)

ELSEVIER

RELX™

[86]   X. Qin, J. Wan, Q. Zhang, Y. Zhang, H. Yu, S. Shi

Carbon Lett., 33 (2023), pp. 781-790